JOURNAL OF SYNCHROTRON RADIATION

ISSN 1600-5775

Received 27 May 2021
Accepted 21 July 2021

Edited by K. Kvashnina, ESRF – The European Synchrotron, France

‡ Present address: Graduate School of Science and Technology, Nara Institute of Science and Technology, 8916-5 Takayama, Ikoma, Nara 630-0192, Japan.

Keywords: soft X-ray ARPES; microbeams; BL25SU; SPring-8.

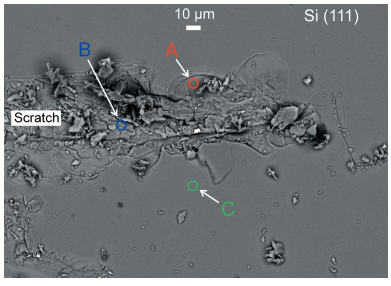

Soft X-ray ARPES for three-dimensional crystals in the micrometre region

Takayuki Muro,[a]* Yasunori Senba,[a] Haruhiko Ohashi,[a] Takuo Ohkochi,[a] Tomohiro Matsushita,[a]‡ Toyohiko Kinoshita[a] and Shik Shin[b]

[a]Japan Synchrotron Radiation Research Institute (JASRI), 1-1-1 Kouto, Sayo, Hyogo 679-5198, Japan, and [b]The Institute for Solid State Physics (ISSP), The University of Tokyo, 5-1-5 Kashiwanoha, Kashiwa, Chiba 277-8581, Japan. *Correspondence e-mail: muro@spring8.or.jp

An endstation dedicated to angle-resolved photoemission spectroscopy (ARPES) using a soft X-ray microbeam has been developed at the beamline BL25SU of SPring-8. To obtain a high photoemission intensity, this endstation is optimized for measurements under the condition of grazing beam incidence to a sample surface, where the glancing angle is 5° or smaller. A Wolter mirror is used for focusing the soft X-rays. Even at the glancing angle of 5°, the smallest beam spot still having a sufficient photon flux for ARPES is almost round on the sample surface and the FWHM diameter is ∼5 μm. There is no need to change the sample orientation for performing $k_x - k_y$ mapping by virtue of the electron lens with a deflector of the photoelectron analyzer, which makes it possible to keep the irradiation area unchanged. A partially cleaved surface area as small as ∼20 μm was made on an Si(111) wafer and ARPES measurements were performed. The results are presented.

1. Introduction

The principle of angle-resolved photoemission spectroscopy (ARPES) presupposes a flat sample surface (Lv *et al.*, 2019). ARPES also requires surface cleanliness in most cases because of the limited probing depth. For these reasons, layered crystals have a technical affinity for ARPES, because flat and clean surfaces can easily be obtained by cleaving. Even for three-dimensional crystals, cleavage is the most convenient way to obtain clean surfaces. Some three-dimensional crystals like rock-salt structure crystals show high cleavability. However, cleavage of three-dimensional crystals often results in very limited and small flat areas with multiple steps or uncleaved areas. Hence, the applicability of ARPES is usually much lower to three-dimensional crystals than to two-dimensional crystals. A promising way to enhance the applicability is to reduce the beam spot size to irradiate partially cleaved areas.

So far, several ARPES endstations using very focused synchrotron radiation in the vacuum ultraviolet (VUV) region have been developed (Dudin *et al.*, 2010; Avila *et al.*, 2013; Rotenberg & Bostwick, 2014; Hoesch *et al.*, 2017). Their beam spots are typically submicrometre in size and, in most cases, sufficiently small for partially cleaved surfaces. However, VUV-ARPES is a surface-sensitive method. To probe bulk electronic states of three-dimensional crystals, soft X-ray ARPES with deeper probing depths is more suitable (Sekiyama *et al.*, 2004; Yokoya *et al.*, 2005; Strocov *et al.*, 2014). Here, we report on a microbeam ARPES endstation developed at the soft X-ray beamline BL25SU (Senba *et al.*, 2016) of SPring-8. The ARPES station previously reported (Muro *et*

al., 2009*a*, 2011), the beam spot size of which was approximately 100 µm, was replaced by this new station. Most of the VUV-ARPES stations use Fresnel zone plates (FZPs). The low transmission efficiency of FZPs, however, is unfavorable for soft X-ray ARPES, because photoionization cross-sections in the soft X-ray region are smaller than those in the VUV region typically by two orders of magnitude (Yeh & Lindau, 1985). In addition, the focal length of an FZP varies depending on the photon energy ($h\nu$), which is frequently changed for k_z dispersion measurements. Thus, we used a focusing mirror called a Wolter mirror (Senba *et al.*, 2020). Furthermore, to enhance the photoemission intensity, we employed a grazing incidence condition where the angle between the beam axis and the sample surface is 5° or smaller (Takata *et al.*, 2005; Strocov, 2013). Even under the grazing incidence condition, the smallest beam spot, which still maintains a photon flux tolerable for ARPES, is almost round on the sample surface and has a diameter of ∼5 µm. In this report, the performances of the soft X-ray microbeam ARPES station are described.

2. Experimental system

The microbeam ARPES system was developed at the soft X-ray beamline BL25SU of SPring-8 (Senba *et al.*, 2016). BL25SU has two branches, Branch A and Branch B, and the microbeam ARPES is located at Branch A. The available $h\nu$ range of Branch A is from 0.12 keV to 2 keV. The resolving powers ($E/\Delta E$) of the monochromator typically used for ARPES are 10 000 to 15 000. The available polarization is circular polarization (Hara *et al.*, 1998).

Fig. 1 shows photographs of the microbeam ARPES station. The focusing mirror is incorporated in the station. Despite the incorporation, the position of the photoelectron analyzer can be independently adjusted to the focal point of the beam. Because the detail of the focusing mirror has already been reported (Senba *et al.*, 2020), our description here is brief: it is a Wolter mirror with a length of 210 mm and a working distance of 250 mm. The Wolter mirror has two different surface regions: ellipsoidal and hyperboloidal regions. The beam is horizontally reflected twice by these surfaces. The measured efficiency of the mirror is ≥ 0.6. Here, the efficiency is defined as the ratio of the flux after the second reflection to that before the first reflection. Since the Wolter mirror is imaging optics, the aberrations are very small. The focused beam size depends on the opening of a four-quadrant slit working as the virtual light source. The blade pair determining the vertical source size is the exit slit, S2a, of the beamline monochromator (Senba *et al.*, 2016). The blade pair determining the horizontal source size, hereafter called the horizontal slit, is placed adjacent to S2a. The previously reported vertical and horizontal FWHM sizes of the focused beam were 0.4 µm and 4 µm, respectively, when using an $h\nu$ of 1000 eV (Senba *et al.*, 2020). We measured the vertical and horizontal sizes at the ARPES station using another $h\nu$ of 750 eV, which is used in this report, and confirmed that they were 0.4 µm and 4 µm, respectively. Here, the vertical and horizontal source sizes were 20 µm and 200 µm, respectively. This S2a opening of 20 µm corresponds to an $E/\Delta E$ of 10 000.

Since the beam is circularly polarized, the photoemission intensity is maximized along the directions perpendicular to the beam direction due to the selection rule of the dipole transition. As seen in Fig. 1, the photoelectron analyzer, DA30

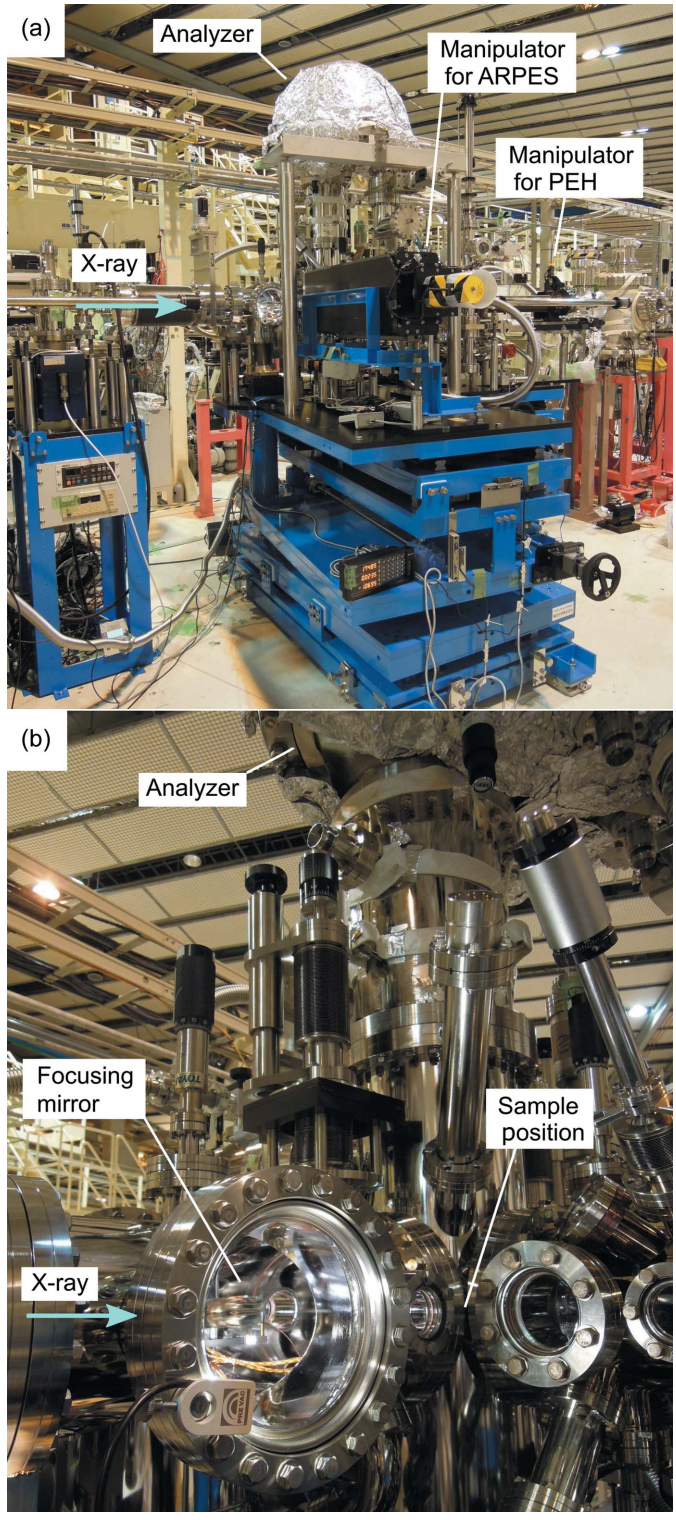

Figure 1
Photographs of the soft X-ray microbeam ARPES endstation.

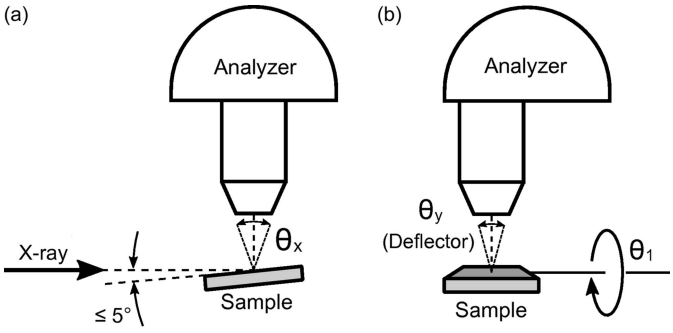

Figure 2
Schematic angular relations between the beam, sample and analyzer: (*a*) side view from the direction perpendicular to the horizontal beam and (*b*) side view from the beam direction. θ_x is the photoemission angle along the longer side direction of the rectangular entrance slit of the hemisphere. θ_y is the deflection angle along the shorter side direction of the slit. The rotation axis θ_1 is used for setting the glancing angle.

of Scienta Omicron, is vertically oriented because it can maximize the photoemission intensity and is also advantageous to the grazing condition described below. As shown in Fig. 2, the glancing angle between the horizontal beam axis and the sample surface is $\leq 5°$. We typically use 5°. When the glancing angle is 5° and the vertical beam size is 0.4 µm, the footprint on the sample is lengthened to 5 µm. Since the horizontal beam size of 4 µm is unchanged, the beam spot on the sample is 5 µm × 4 µm in size. Despite the grazing condition, the footprint is almost round. This beam spot was used for the ARPES measurements in Section 3.3. The horizontal beam size of 4 µm was obtained when the opening of the horizontal slit was 200 µm. When we do not need the smallest beam spot, we fully open the horizontal slit to around 1 mm. This increases the photon flux by ∼5 times. In this case, the measured vertical and horizontal beam sizes were 0.5 µm and 13 µm, respectively. Here, the S2a opening was 20 µm. When the glancing angle is 5°, the beam spot on the sample becomes 6 µm × 13 µm in size. This beam spot was used in Section 3.2.

As indicated by the orientation of the analyzer hemisphere in Fig. 2, the longer side of the rectangular-shaped entrance slit of the hemisphere is directed in parallel with the horizontal beam axis. As is common for this type of analyzer, the DA30 analyzer can simultaneously analyze photoelectrons angularly dispersed along the longer side direction of the slit. This angle is denoted by θ_x in Fig. 2(*a*). The acceptable sector angle is ±15°. For convenience of explanation, we call this sector plane the original plane. In addition, by using the deflector, the DA30 analyzer can also simultaneously analyze angularly dispersed photoelectrons in a plane tilted from the original plane toward the shorter side direction of the slit by at most ±10°. The deflection angle is denoted by θ_y in Fig. 2(*b*). Note that the acceptable sector angle becomes smaller with increasing deflection angle. By scanning the deflection angle, two-dimensional angular mapping can be performed. The mapping area of ±15° × ±10° is large enough to cover the first Brillouin zone when using soft X-rays. Consequently, ARPES measurements can be performed without changing the relative angle between the analyzer and the sample. In other words, the sample can stay at the same position during measurements. This enables us to keep the footprint size of the beam and the irradiation position on the sample.

The sample can be cooled by a liquid helium flow cryostat. The available temperatures, which are measured by a sensor mounted on the back side of the sample holder, range from 6 K to room temperature. The sample is usually glued on a copper substrate and then the substrate is screwed on a sample carrier similar to the one previously reported (Muro *et al.*, 2009*a*, 2011). The sample carrier is transferred from an airlock chamber to the sample holder in the measurement chamber. The sample holder can be tightened by *in situ* screwing to increase the thermal contact (Muro *et al.*, 2011). The cooled sample can be cleaved by using a wobble stick. The sample manipulator is a stepping motor-controlled manipulator composed of one rotation and three linear motion axes. The rotation axis corresponds to θ_1 in Fig. 2(*b*). Because we gave priority to the lowest temperature, the sample manipulator does not have azimuth rotation capability. Thus, the azimuth angle should be oriented when the sample is mounted on the sample carrier.

To assist in selecting a nicely cleaved flat area from a poorly cleaved sample surface, the station is equipped with a high-magnification optical camera observing the sample surface from the beam propagation direction (Muro *et al.*, 2009*b*). Fig. 3 schematically describes the observation method. As shown in Fig. 3(*b*), the camera observes the sample via a plane mirror with a tunnel through which the beam can pass. The camera lens is placed outside the vacuum chamber and the working distance is 325 mm. The plane mirror is located between the Wolter mirror and sample. As shown in Fig. 3(*a*), the sample is illuminated with visible light in such a way that the surface shines in the camera view when the angle between the surface and the soft X-ray beam is 5°. Thus, when we want to find surface areas cleaved well in parallel with the substrate surface, we first set the angle of the substrate surface at 5° with respect to the soft X-ray beam. Then, we find shiny areas in the camera view. Dark areas are not in parallel with the substrate. Here, it is assumed that the cleavable plane of the sample is oriented in parallel with the substrate surface beforehand. Finally, a selected shiny area is positioned at the beam spot marked in the camera view (Muro *et al.*, 2009*b*).

It is important to adjust the electron lens axis of the DA30 analyzer to the focal point of the beam by horizontally moving the analyzer along the beam direction. As already mentioned,

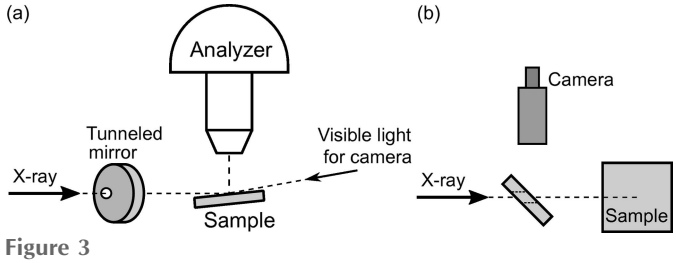

Figure 3
Schematic of the camera system observing the sample along the beam direction: (*a*) side view from the direction perpendicular to the beam and (*b*) top view, where the analyzer is not shown.

the position of the analyzer can independently be adjusted with respect to the beam focus. The electron lens has a transmission mode in addition to the angular mode. When the transmission mode is used and the lens axis is adjusted to a beam spot on a sample, photoelectrons converge at the middle of the two-dimensional detector. The beam focus can be found using a knife-edge mounted at the end of the sample holder. Thus, the lens axis can be adjusted to the beam focus by positioning the analyzer in such a way that the photoelectrons emitted from the knife-edge placed at the beam focus converge at the middle of the detector. When we want to position a surface area on a sample to the beam focus, we first place the surface area in the beam path by using the camera in Fig. 3. Then, we adjust the sample position along the beam direction so that the photoelectrons are detected at the middle of the detector.

In this paragraph, we mention another capability of this endstation for photoelectron diffraction or photoelectron holography (PEH) (Matsushita *et al.*, 2010), although it deviates from the main topic of this report on ARPES. The measurement chamber is equipped with another sample manipulator for PEH as schematically shown in Fig. 4. This manipulator has theta and azimuth rotation axes denoted by θ_2 and φ, respectively. The only available sample temperature is room temperature. The θ_2 axis is in parallel with the beam axis. The angle between the beam axis and the φ axis is 85°. Thus, the glancing angle is always kept at 5°, maintaining a high photoemission intensity. Unlike ARPES, the angular mapping by the DA30 analyzer is too narrow for PEH. Thus, we usually perform the DA30 angular mapping at different θ_2 and φ angles and then combine the maps analytically into a photoelectron hologram of a large solid angle (Matsushita *et al.*, 2020). Some photoelectron holograms obtained by this method have already been reported (Tsutsui *et al.*, 2017; Yokoya *et al.*, 2019). In these reports, by taking advantage of the high photoemission intensity, photoelectron holograms of dopants in semiconductors were successfully observed for each chemically shifted core-level photoemission peak resolved by the high-energy-resolution DA30 analyzer. In other words, site-selective PEH was performed. For PEH measurements, homogeneous sample surfaces are presupposed, because it is difficult to maintain the irradiation area when changing the θ_2 and φ angles.

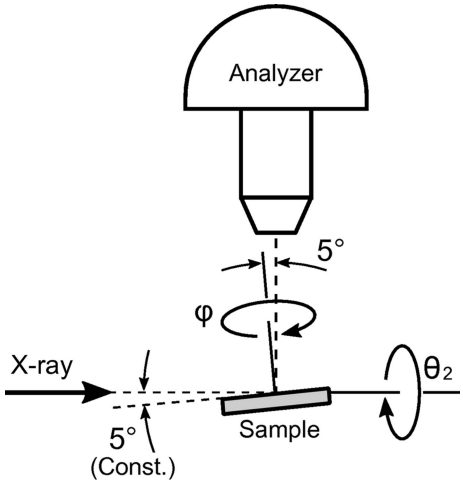

Figure 4
Schematic side view of the station including the sample manipulator for photoelectron diffraction or photoelectron holography. The glancing angle of 5° is constant. The θ_2 rotation axis is parallel to the beam axis. The angle between the beam axis and the φ rotation axis is 85°.

3. Results and discussion

3.1. Effect of grazing incidence

To confirm the effectiveness of the grazing incidence condition, we measured the dependence of the photoemission intensity on the glancing angle. An Si(111) wafer with a native oxide surface layer was used for the sample. The value of $h\nu$ of the excitation beam was 750 eV. The total energy resolution (ΔE) was 90 meV. The cross-sectional beam sizes at the sample position were 0.4 µm and 4 µm in the vertical and horizontal directions, respectively. The sample was at room temperature. Fig. 5(*a*) shows the angle-integrated photoemission spectrum of the Si 2*p* core level measured at the glancing angle [*i.e.* the angle between the beam axis and the Si(111) surface] of 45°. In Fig. 5(*b*), relative photoemission intensities measured at different glancing angles are plotted. The glancing angle was adjusted by the θ_1 rotation indicated in Fig. 2(*b*). The plotted intensities are the Si 2*p* photoemission intensities integrated in the binding energy (E_B) range from 98.6 eV to 106.6 eV including the photoemission peaks of the bulk Si and SiO_2. The photoemission intensity at a glancing angle of 5° is 16 times higher than that at 45°. The glancing angle of our previous ARPES station was typically 45° (Muro *et al.*, 2009*a*, 2011). Therefore, the photoemission intensity is improved by one order of magnitude compared with the previous station. As shown in Fig. 5(*b*), the photoemission intensity increases further with decreasing angle and peaks at 2°. The photoemission intensity at 2° is 72 times higher than that at 45°. Even at 2°, the lengthened vertical spot size on the sample surface is still so small as not to affect the angular resolution of the analyzer. In fact, valence band dispersions were clearly observed for the same sample at a glancing angle of 2° as shown in Fig. 5(*c*). Here, we used vertical and horizontal beam sizes of 0.5 µm and 13 µm, respectively, Thus, the vertical spot size on the sample was 14 µm. Note that any surface cleaning was not performed before the measurements. Nevertheless, the dispersions of the bulk Si under the surface native oxide were observed by virtue of the relatively deep probing depth of soft X-ray ARPES (Strocov *et al.*, 2014). It should be mentioned that the glancing angle maximizing the photoemission intensity depends on the sample and $h\nu$ (Strocov, 2013).

3.2. ARPES on the side plane of an Si wafer

As an example of a relatively large cleaved surface, we used the side plane of an Si($1\bar{1}0$) wafer. The Si wafer with a thickness of 0.5 mm was mounted on a substrate in a standing posture as schematically described in Fig. 6(*a*). Here, we oriented the [111] direction perpendicular to the substrate

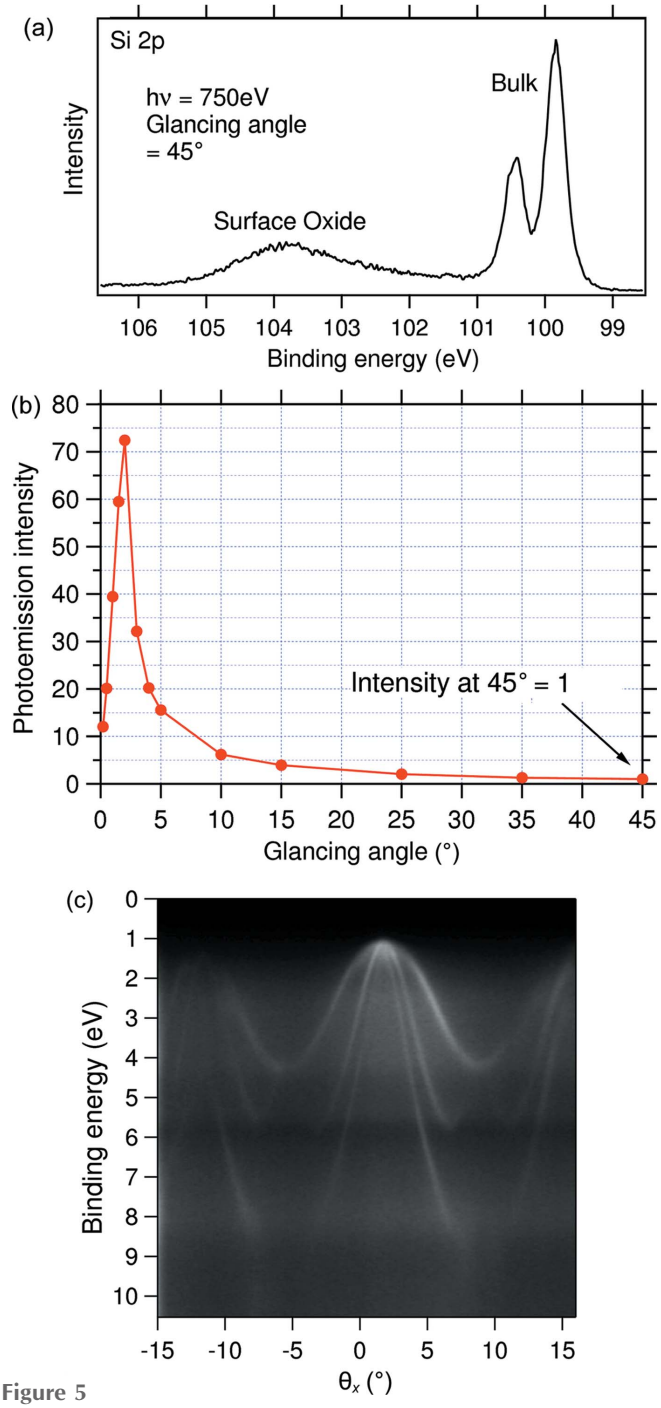

Figure 5
(*a*) Angle-integrated Si 2*p* core-level photoemission spectrum measured for an Si(111) wafer with native surface oxide. The glancing angle was 45°. (*b*) Photoemission intensities at different glancing angles relative to the intensity at 45°. Each intensity was obtained by integrating the Si 2*p* spectrum measured at each angle over the whole energy range in (*a*). (*c*) Valence band dispersions along the Γ–*X* direction measured for the same sample with a glancing angle of 2°, where the photoemission intensity was maximized. Here, θ_x is the angle along the longer side of the rectangular slit of the analyzer as indicated in Fig. 2. For all the measurements in this figure, $h\nu$ was 750 eV, the total ΔE was 90 meV and the sample was at room temperature.

surface, because the Si(111) plane is a cleavable plane. Then, the Si wafer was cooled and cleaved *in situ* under a base pressure of 2×10^{-8} Pa. The glancing angle between the beam

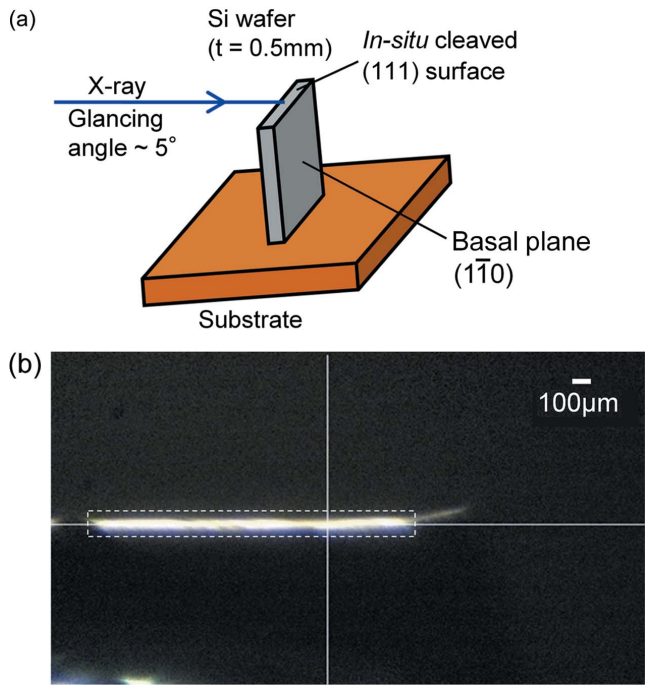

Figure 6
(*a*) Schematic of mounting an Si(1$\bar{1}$0) wafer with a thickness of 0.5 mm. The (111) side plane cleaved *in situ* was used for ARPES measurements. The glancing angle was 5°. (*b*) View of the camera described in Fig. 3. The intersection of the white cross lines indicates the beam position. The bright area indicated by a dashed rectangle is the well cleaved (111) surface illuminated by the visible light described in Fig. 3.

and the Si(111) cleaved surface was set to 5°. Fig. 6(*b*) is the view of the camera described in Fig. 3. The shiny area is the well cleaved surface. The cleaved surface was adjusted to the beam focus by the method already explained. First, we performed the DA30 angular mapping. The value of $h\nu$ was 750 eV. The footprint size on the sample was 6 μm × 13 μm. The total ΔE was 90 meV. The sample temperature was 86 K. The deflection angle (θ_y) of the DA30 analyzer was scanned from −10° to +10° in 0.2° steps. The total measurement time was 40 min. Fig. 7(*a*) shows band dispersions measured at two representative deflection angles. A mesh pattern caused by the mesh electrode in front of the two-dimensional detector is seen in Fig. 7(*a*), because the energy-fixed mode of the DA30 analyzer was used. Fig. 7(*b*) shows constant energy cuts of the measured dispersions at two representative E_Bs, corresponding to $k_x - k_y$ maps. The energy window is 200 meV. From the constant energy cuts, it was found that the Γ point is located at a deflection angle of +0.5°. Then, we set the deflection angle at +0.5° and measured the dispersions again using the energy scan mode to remove the mesh pattern. Fig. 8 shows the results. Here, the time dependence of the data accumulation is also shown. The dispersions were observed in 12 min with sufficient data quality.

3.3. ARPES on a small cleaved area

To demonstrate ARPES measurements on a partially cleaved surface, we used the basal plane of an Si(111) wafer

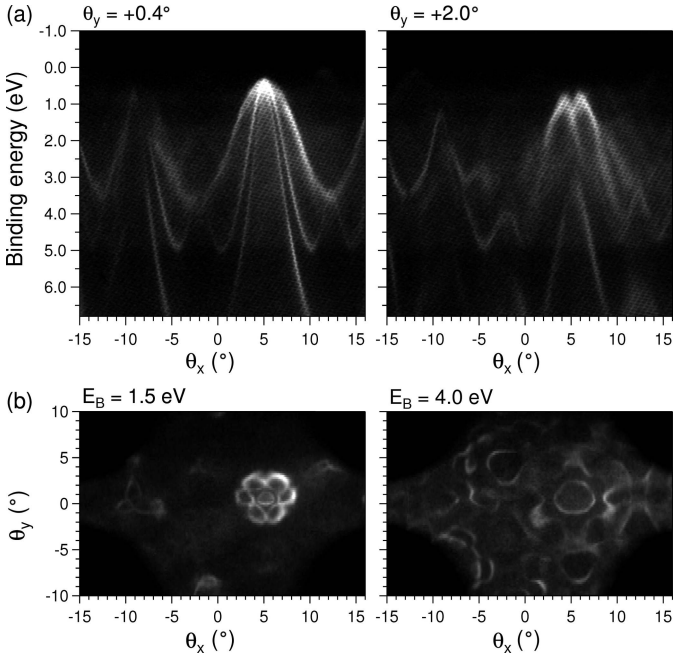

Figure 7
Results of the DA30 angular mapping performed for the Si wafer described in Fig. 6. The value of $h\nu$ was 750 eV. The total ΔE was 90 meV. The sample temperature was 86 K. The energy-fixed mode of the DA30 analyzer was used. The total measurement time was 40 min. (*a*) Valence band dispersions at two representative deflection angles of +0.4° and +2.0°. (*b*) Constant energy cuts at two representative E_Bs of 1.5 eV and 4.0 eV. The energy window is 200 meV. Here, θ_y is the deflection angle along the shorter side of the rectangular slit of the analyzer as indicated in Fig. 2.

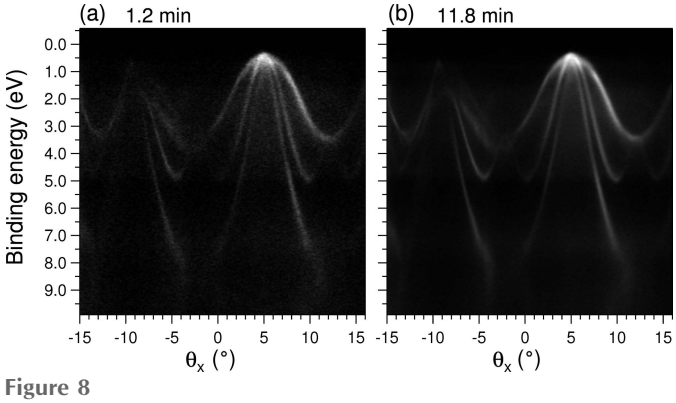

Figure 8
Valence band dispersions along the Γ–*X* direction measured for the Si wafer described in Fig. 6. The value of θ_y was +0.5° and $h\nu$ was 750 eV. The total ΔE was 90 meV. The sample temperature was 86 K. The energy scan mode of the DA30 analyzer was used. (*a*) Result after one energy scan; the measurement time was 1.2 min. (*b*) Result after ten energy scans; the measurement time was 11.8 min. Note that the Si($1\bar{1}0$) wafer used here is different from the Si(111) wafer used in Fig. 5(*c*). The smaller E_B at the valence top in this figure by ∼0.8 eV compared with the valence top in Fig. 5(*c*) is probably due to the difference in doping conditions.

shown in Fig. 9(*a*). As shown in Fig. 5(*c*), band dispersions are observable even with native surface oxide. To make dispersions unobservable on non-cleaved areas, we intentionally polished the surface with a #15000 polishing sheet under air. The polished Si(111) wafer was transferred to the measurement chamber and cooled. Then, to create small cleaved areas,

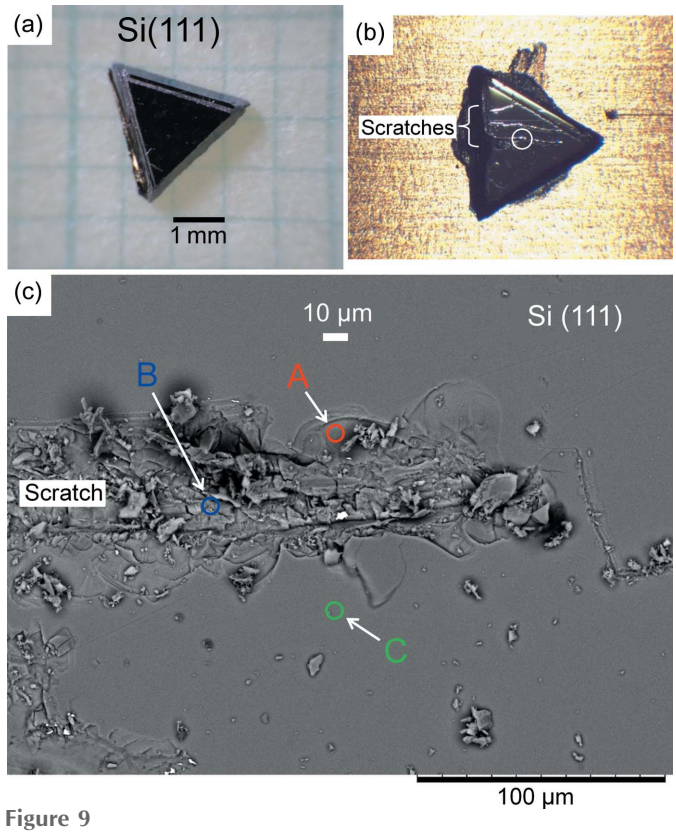

Figure 9
(*a*) Optical microscope image of the Si(111) wafer before the ARPES measurements. (*b*) Optical microscope image of the Si(111) wafer after scratching the surface *in situ*. Note that this image was observed not by the camera in Fig. 3 but by another camera mounted on a viewport. (*c*) SEM image of the Si(111) wafer observed *ex situ* after the ARPES measurements. Positions A, B, and C indicate the positions at which the ARPES measurements were performed. Position A is a cleaved area ∼20 μm in size. Position B is a scratched area. Position C is a pristine area. Note that the pristine surface before scratching was polished with a fine polishing sheet under air so that any dispersions were not observed on the pristine surface.

the surface was scratched *in situ* with a diamond file under a base pressure of 2×10^{-8} Pa. Fig. 9(*b*) shows the scratched Si(111) wafer placed in the measurement chamber. Fig. 9(*c*) is an image taken *ex situ* by a scanning electron microscope (SEM). As observed in Fig. 9(*c*), a lot of small cleaved areas with sizes of a few tens of micrometres were made beside the scratch. We performed ARPES measurements on the cleaved area, the scratch and the polished surface, as indicated in Fig. 9(*c*). The value of $h\nu$ was 750 eV. The glancing angle was 5°. The footprint size on the sample was 5 μm × 4 μm. The total ΔE was 90 meV. The sample temperature was 80 K. The scratch was observable by the camera of Fig. 3. However, the resolution of the camera was not high enough to identify the cleaved area. Therefore, we found the cleaved area with the help of Si 2*p* core-level photoemission spectra. The SiO_2 peak seen in Fig. 5(*a*) disappeared on the cleaved area as shown in Fig. 10(*a*). The SiO_2 peak was also not observed on the scratch as shown in Fig. 10(*b*), but the Si bulk peaks became broader probably due to the surface roughness. On the polished surface in Fig. 10(*c*), a large SiO_2 peak was observed, because the surface was polished under air. Fig. 11

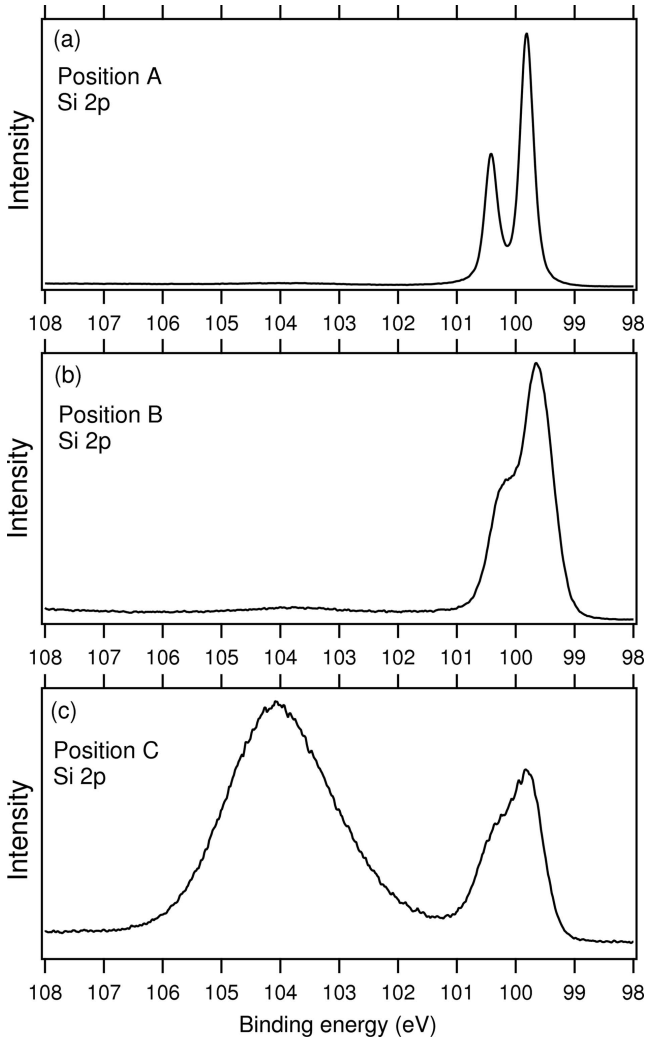

Figure 10
Angle-integrated Si 2*p* photoemission spectra measured at (*a*) position A, (*b*) position B and (*c*) position C on the Si(111) wafer in Fig. 9(*c*). The value of $h\nu$ was 750 eV. The total ΔE was 90 meV. The sample temperature was 80 K. The beam spot on the sample was 5 µm × 4 µm in size.

shows the results of the DA30 angular mapping on the cleaved area using the energy-fixed mode. By virtue of the deflector, the $k_x - k_y$ mapping was able to be performed without changing the irradiation area. Then, we measured the band dispersions using the energy scan mode. The deflection angle was +1°. Fig. 12(*a*) shows the result. The same measurements were also performed on the scratch and the polished surface as shown in Figs. 12(*b*) and 12(*c*), respectively. As expected, clear band dispersions were observed only on the cleaved area. These results indicate the effectiveness of the microbeam ARPES station for three-dimensional crystals, even when successfully cleaved areas are very partial and as small as a few tens of micrometres.

4. Conclusions

We developed a soft X-ray microbeam ARPES endstation at the beamline BL25SU of SPring-8. The grazing incidence of the soft X-ray beam to the sample surface enhanced the photoemission intensity by one order of magnitude compared with the previous ARPES endstation at BL25SU. The vertical size of the focused beam cross section is <1 µm and much smaller than the horizontal size. Therefore, although the vertical size is lengthened by the grazing incidence, the footprint on the sample surface is almost round. We performed demonstrative ARPES measurements using a round shape footprint with a diameter of ∼5 µm at a glancing angle of 5°. On a partially cleaved area as small as ∼20 µm, which was made on an Si(111) wafer, clear band dispersions were observed. $k_x - k_y$ maps were also measured maintaining the irradiation to the small cleaved area by virtue of the deflector of the photoelectron analyzer. In many cases, it is difficult to cleave single-crystal samples with three-dimensional crystal structures and cleavage attempts often result in very partial and small cleaved areas. We expect that the developed microbeam ARPES endstation facilitates ARPES measurements of three-dimensional crystals. At present, a horizontal beam size of 4 µm can be achieved with a reduced horizontal slit opening. However, the horizontal beam size will become

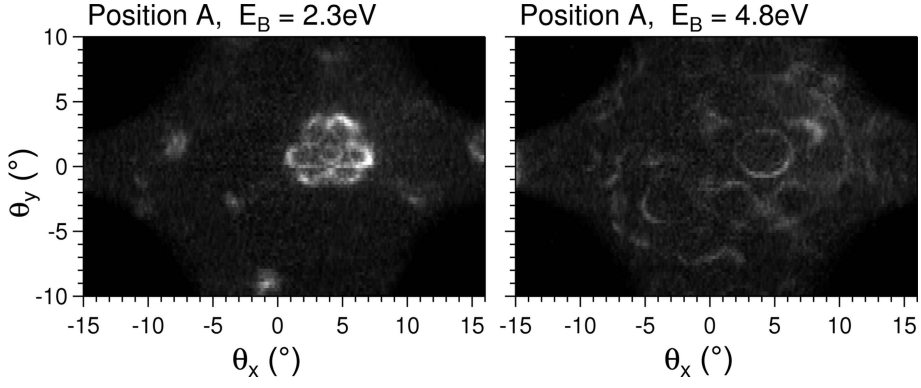

Figure 11
Constant energy cuts at two representative E_Bs measured at position A on the Si(111) surface indicated in Fig. 9(*c*). The energy fixed mode of the DA30 analyzer was used. The value of $h\nu$ was 750 eV. The total ΔE was 90 meV. The sample temperature was 80 K. The beam spot on the sample was 5 µm × 4 µm in size.

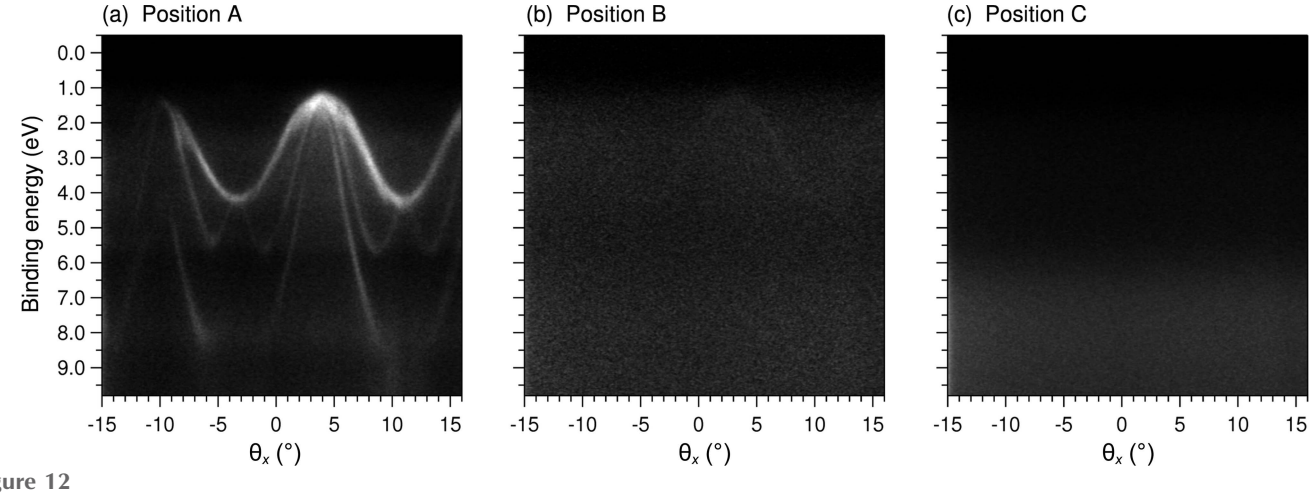

Figure 12
Results of band dispersion measurements along the Γ–*X* direction at (*a*) position A, (*b*) position B and (*c*) position C on the Si(111) surface indicated in Fig. 9(*c*). θ_y was +1°. The energy scan mode of the DA30 analyzer was used. The value of $h\nu$ was 750 eV. The total ΔE was 90 meV. The sample temperature was 80 K. The beam spot on the sample was 5 µm × 4 µm in size.

~1 µm or smaller even without reducing the horizontal slit opening when a diffraction-limited light source in the soft X-ray region is realized by the SPring-8 upgrade planned in the future.

Acknowledgements

The authors are grateful to Takayuki Kiss for his valuable advice on the adjustment of the photoelectron analyzer. The authors also thank Xeniya Kozina, Yoshinori Kotani and Tetsuya Nakamura for their support on the ARPES endstation development and beamline experiments. One of the authors (T. Muro) thanks Kentaro Toyoki for his support on the SEM observation.

Funding information

This work was supported by Photon and Quantum Basic Research Coordinated Development Program from MEXT. This work was also partially supported by JSPS KAKENHI (Grant Nos. JP23600017, JP26105001, JP26105007). The synchrotron radiation experiments were performed with the approval of JASRI (Proposal Nos. 2014B1498, 2015B2002, 2016A1844, 2017B1258, 2017B1982, 2018A1283, 2018A2064, 2018B2103, 2019A1323, 2019A2067, 2019B2028, 2020A2048).

References

Avila, J., Razado-Colambo, I., Lorcy, S., Lagarde, B., Giorgetta, J.-L., Polack, F. & Asensio, M. C. (2013). *J. Phys. Conf. Ser.* **425**, 192023.
Dudin, P., Lacovig, P., Fava, C., Nicolini, E., Bianco, A., Cautero, G. & Barinov, A. (2010). *J. Synchrotron Rad.* **17**, 445–450.
Hara, T., Tanaka, T., Tanabe, T., Mareéchal, X.-M., Kumagai, K. & Kitamura, H. (1998). *J. Synchrotron Rad.* **5**, 426–427.
Hoesch, M., Kim, T. K., Dudin, P., Wang, H., Scott, S., Harris, P., Patel, S., Matthews, M., Hawkins, D., Alcock, S. G., Richter, T., Mudd, J. J., Basham, M., Pratt, L., Leicester, P., Longhi, E. C., Tamai, A. & Baumberger, F. (2017). *Rev. Sci. Instrum.* **88**, 013106.
Lv, B., Qian, T. & Ding, H. (2019). *Nat. Rev. Phys.* **1**, 609–626.
Matsushita, T., Matsui, F., Daimon, H. & Hayashi, K. (2010). *J. Electron Spectrosc. Relat. Phenom.* **178–179**, 195–220.
Matsushita, T., Muro, T., Matsui, F., Happo, N. & Hayashi, K. (2020). *Jpn. J. Appl. Phys.* **59**, 020502.
Muro, T., Kato, Y., Kinoshita, T. & Watanabe, Y. (2009*b*). *J. Synchrotron Rad.* **16**, 595–596.
Muro, T., Kato, Y., Matsushita, T., Kinoshita, T., Watanabe, Y., Okazaki, H., Yokoya, T., Sekiyama, A. & Suga, S. (2011). *J. Synchrotron Rad.* **18**, 879–884.
Muro, T., Kato, Y., Matsushita, T., Kinoshita, T., Watanabe, Y., Sekiyama, A., Sugiyama, H., Kimura, M., Komori, S., Suga, S., Okazaki, H. & Yokoya, T. (2009*a*). *Rev. Sci. Instrum.* **80**, 053901.
Rotenberg, E. & Bostwick, A. (2014). *J. Synchrotron Rad.* **21**, 1048–1056.
Sekiyama, A., Kasai, S., Tsunekawa, M., Ishida, Y., Sing, M., Irizawa, A., Yamasaki, A., Imada, S., Muro, T., Saitoh, Y., Onuki, Y., Kimura, T., Tokura, Y. & Suga, S. (2004). *Phys. Rev. B*, **70**, 060506.
Senba, Y., Kishimoto, H., Takeo, Y., Yumoto, H., Koyama, T., Mimura, H. & Ohashi, H. (2020). *J. Synchrotron Rad.* **27**, 1103–1107.
Senba, Y., Ohashi, H., Kotani, Y., Nakamura, T., Muro, T., Ohkochi, T., Tsuji, N., Kishimoto, H., Miura, T., Tanaka, M., Higashiyama, M., Takahashi, S., Ishizawa, Y., Matsushita, T., Furukawa, Y., Ohata, T., Nariyama, N., Takeshita, K., Kinoshita, T., Fujiwara, A., Takata, M. & Goto, S. (2016). *AIP Conf. Proc.* **1741**, 030044.
Strocov, V. N. (2013). *J. Synchrotron Rad.* **20**, 517–521.
Strocov, V. N., Wang, X., Shi, M., Kobayashi, M., Krempasky, J., Hess, C., Schmitt, T. & Patthey, L. (2014). *J. Synchrotron Rad.* **21**, 32–44.
Takata, Y., Yabashi, M., Tamasaku, K., Nishino, Y., Miwa, D., Ishikawa, T., Ikenaga, E., Horiba, K., Shin, S., Arita, M., Shimada, K., Namatame, H., Taniguchi, M., Nohira, H., Hattori, T., Södergren, S., Wannberg, B. & Kobayashi, K. (2005). *Nucl. Instrum. Methods Phys. Res. A*, **547**, 50–55.
Tsutsui, K., Matsushita, T., Natori, K., Muro, T., Morikawa, Y., Hoshii, T., Kakushima, K., Wakabayashi, H., Hayashi, K., Matsui, F. & Kinoshita, T. (2017). *Nano Lett.* **17**, 7533–7538.
Yeh, J. J. & Lindau, I. (1985). *At. Data Nucl. Data Tables*, **32**, 1–155.
Yokoya, T., Nakamura, T., Matsushita, T., Muro, T., Takano, Y., Nagao, M., Takenouchi, T., Kawarada, H. & Oguchi, T. (2005). *Nature*, **438**, 647–650.
Yokoya, T., Terashima, K., Takeda, A., Fukura, T., Fujiwara, H., Muro, T., Kinoshita, T., Kato, H., Yamasaki, S., Oguchi, T., Wakita, T., Muraoka, Y. & Matsushita, T. (2019). *Nano Lett.* **19**, 5915–5919.